論文 / 著書情報
Article / Book Information

Title	Rigorous electromagnetic simulator for extreme ultraviolet lithography and convolutional neural network reproducing electromagnetic simulations
Authors	Hiroyoshi Tanabe, Masayuki Shimoda, Atsushi Takahashi
Citation	Journal of Micro/Nanopatterning, Materials and Metrology (JM3)
Pub. date	2025, 5
DOI	https://doi.org/10.1117/1.JMM.24.2.024201
Rights	(Copyright) CC BY: (c) The Authors. Published by SPIE under a Creative Commons Attribution 4.0 International License (See next page.).Distribution or reproduction of this work in whole or in part requires full attribution of the original publication, including its DOI. [https://doi.org/10.1117/1.JMM.24.2.024201] (Citation) Hiroyoshi Tanabe, Masayuki Shimoda, and Atsushi Takahashi "Rigorous electromagnetic simulator for extreme ultraviolet lithography and convolutional neural network reproducing electromagnetic simulations",Journal of Micro/Nanopatterning, Materials, and Metrology 24(2), 024201 (11 May 2025).https://doi.org/10.1117/1.JMM.24.2.024201

License

JM3 Journal of Micro/Nanopatterning, Materials, and Metrology

RESEARCH PAPER

Rigorous electromagnetic simulator for extreme ultraviolet lithography and convolutional neural network reproducing electromagnetic simulations

Hiroyoshi Tanabe,* Masayuki Shimoda, and Atsushi Takahashi
Institute of Science Tokyo, Tokyo, Japan

ABSTRACT. **Background:** Mask 3D (M3D) effects distort diffraction amplitudes from extreme ultraviolet (EUV) masks. Rigorous electromagnetic simulation is required to incorporate the M3D effects. However, electromagnetic simulation is too slow for optical proximity correction applications.

Aim: We explain the details of our electromagnetic simulator and convolutional neural network (CNN) model which reproduces the results of the electromagnetic simulations. CNN prediction is much faster than the simulation. We provide the codes for the simulator and CNN model.

Approach: Our electromagnetic simulator uses the 3D waveguide model. The model solves Helmholtz-type wave equations. Weakly guiding approximation is applied to accelerate the simulation. M3D parameters are extracted from the result of the simulation, which represents the M3D effects. CNN model is constructed to predict M3D parameters from the input mask pattern.

Results: The computation time of the electromagnetic simulation is ~5 min for a 512×512 nm area on a wafer. The computation time using CNN is ~0.1 s.

Conclusions: EUVlitho is the open source of our EUV lithography simulator and CNN model. It is available on GitHub.

Keywords: lithography simulation; neural network; extreme ultraviolet mask

Paper 24094G received Dec. 18, 2024; revised Mar. 18, 2025; accepted Apr. 15, 2025; published May 11, 2025.

1 Introduction

High aspect absorbers used in extreme ultraviolet (EUV) masks induce several mask 3D (M3D) effects such as critical dimension (CD) error and edge placement error.[1,2] It is necessary to include M3D effects in EUV lithography simulations. M3D effects are caused by the distorted diffraction amplitude from an EUV mask. The diffraction amplitude can be calculated rigorously by using electromagnetic (EM) simulators.[3–7] There are two types of EM simulation methods for EUV lithography. The first type solves Maxwell's equations in coordinate space,[3] and the second type solves the equations in momentum (or frequency) space.[4–7] The differential Maxwell's equations in coordinate space are transformed into coupled wave equations in momentum space.

The finite-difference time-domain (FDTD) method[3] solves Maxwell's equations in coordinate space, and the solution is the near-field diffraction amplitude. Because the near-field diffraction amplitude depends on the incident angle, the calculation must be repeated for all source points (usually 100 or more).

*Address all correspondence to Hiroyoshi Tanabe, tanabe@eda.ict.eng.isct.ac.jp

On the other hand, rigorous coupled-wave analysis (RCWA)[4] and 3D waveguide model[5–7] solve Maxwell's equation in momentum space. Both models are equivalent, but the 3D waveguide model has fewer variables.[7] Assuming a periodic boundary condition, the momentum is discretized proportional to the inverse of the period length. RCWA and 3D waveguide models solve coupled wave equations that connect the incoming and outgoing waves. All relationships between the incoming and outgoing waves are calculated simultaneously. The momentum of the incoming wave corresponds to the source point. If the period length is large enough, the size of the momentum grid is small, and these models do not need to repeat calculations for different source points (Fig. 2).

In this paper, we explain our EM simulator based on the 3D waveguide model. The theoretical background of the 3D waveguide model was presented in the previous paper.[7] In this report, we explain the details of the 3D waveguide model calculation. The model solves Helmholtz-type coupled vector wave equations. Weakly guiding approximation in optical fiber theory[8] is applied to the 3D waveguide model, which decomposes the coupled vector wave equations into two scalar wave equations, reducing the computation time to solve the equations.

Rigorous EM simulations such as FDTD, RCWA, and 3D waveguide models are highly time-consuming, especially for optical proximity correction (OPC) applications. Recently with the advent of deep learning software and hardware platforms, several attempts have been made to solve the M3D effect problems using deep neural networks.[9–11] The targets of the deep neural networks in these models are the near-field diffraction amplitudes calculated by FDTD. As mentioned before, the near-field amplitudes depend on the incident angles, and the calculations of the amplitudes need to be repeated for many (if not all) source points.

We also use a deep neural network to accelerate the calculation of M3D effects. We define the M3D amplitudes as the difference between the far-field diffraction amplitudes calculated by the 3D waveguide model and the thin mask amplitude calculated by the Fourier transformation of the mask pattern. We construct a convolutional neural network (CNN),[12–15] which reproduces the M3D amplitudes. Because the far-field diffraction amplitude is expressed in momentum space, our model can be easily incorporated into the Hopkins' TCC (transmission cross-coefficient) formula,[16] which is also written in momentum space. In this way, we do not need to repeat the calculations for different source points.

In Sec. 2, we explain our EUV lithography simulator based on the 3D waveguide model. In Sec. 3, we explain the linear approximation of the diffracted electric field. In Sec. 4, we explain our CNN model for fast EUV lithography simulation. Section 5 is the summary.

2 EUV Lithography Simulator

2.1 Image Intensity on a Wafer

According to Abbe's theory, the total image intensity on a wafer, I is calculated by the incoherent sum of the image intensities illuminated by all points of the effective source, S as follows:

$$I(x,y)=\iint S(s_x,s_y)\left|\iint \boldsymbol{E}(\boldsymbol{k}_{\text{out}};\boldsymbol{k}_{\text{in}})P(p_x,p_y)e^{i(p_x x+p_y y)}\mathrm{d}p_x\,\mathrm{d}p_y\right|^2\mathrm{d}s_x\,\mathrm{d}s_y, \tag{1}$$

where P is the pupil function of the projection optics. The electric field $\boldsymbol{E}$ diffracted by a EUV mask is calculated by solving the 3D waveguide model in Sec. 2.2. It depends on the incoming momentum $\mathbf{k}_{\text{in}}$ and the outgoing momentum $\mathbf{k}_{\text{out}}$. These are calculated using the source position of the incoming wave (s_x,s_y) and the pupil position of the outgoing wave (p_x,p_y) as follows:

$$\boldsymbol{k}_{\text{in}}=\left(s_x+k\sin\theta\sin\varphi,s_y+k\sin\theta\cos\varphi,\sqrt{k^2-(s_x+k\sin\theta\sin\varphi)^2-(s_y+k\sin\theta\cos\varphi)^2}\right), \tag{2}$$

$$\boldsymbol{k}_{\text{out}}=\left(p_x+k\sin\theta\sin\varphi,p_y+k\sin\theta\cos\varphi,-\sqrt{k^2-(p_x+k\sin\theta\sin\varphi)^2-(p_y+k\sin\theta\cos\varphi)^2}\right), \tag{3}$$

where $k=2\pi/\lambda$ is the wavevector with the wavelength $\lambda=13.5$ nm. The optics of EUV scanners are reflective, and the chief ray is tilted $\theta=-6$ deg in the negative y direction. The

illumination slit of EUV scanners is curved. The azimuthal angle φ is 0 deg at the center of the slit. The angle is ~18 deg[17] at the edge of the slit.

The pupil function P includes the defocus and the aberrations. In this report, we assume the pupil function is a scalar function because the numerical aperture (NA) = 0.33. However, for high-NA scanners, the pupil function becomes a matrix that rotates the electric field from the entrance pupil to the exit pupil.[18]

2.2 3D Waveguide Model with Weakly Guiding Approximation

EUV masks have absorber layers on the top of the Ru capping layer and Mo/Si multilayers (ML). Inside each layer the complex dielectric constant $\hat{\varepsilon}$ is uniform in the z direction, which is perpendicular to the mask plane. In this case, according to the 3D waveguide model,[5] Maxwell's equations are reduced to the following coupled wave equations of the vector potential $\boldsymbol{A}$.

$$\Delta A_x + k^2 \hat{\varepsilon} A_x - \frac{\partial \log \hat{\varepsilon}}{\partial x}\left(\frac{\partial A_x}{\partial x} + \frac{\partial A_y}{\partial y}\right) = 0, \tag{4}$$

$$\Delta A_y + k^2 \hat{\varepsilon} A_y - \frac{\partial \log \hat{\varepsilon}}{\partial y}\left(\frac{\partial A_x}{\partial x} + \frac{\partial A_y}{\partial y}\right) = 0, \tag{5}$$

$$A_z = 0. \tag{6}$$

The electric field and the magnetic field are calculated from the vector potential as follows:

$$\boldsymbol{E} = ik\boldsymbol{A} + \frac{\mathrm{i}}{k}\nabla\left(\frac{1}{\hat{\varepsilon}}\nabla \cdot \boldsymbol{A}\right), \tag{7}$$

$$\boldsymbol{H} = \nabla \times \boldsymbol{A}. \tag{8}$$

The coupled wave equations are decoupled by using the weakly guiding approximation,[7] which is often used in optical fiber theory.[8] This approximation is possible because the refractive index of the core is close to that of the cladding. Similarly, the refractive index of Ta absorber, $(n, k) = \sqrt{\hat{\varepsilon}} = (0.9567, 0.0343)$,[19] is close to that of the vacuum. The weakly guiding approximation decomposes the coupled vector wave equations into uncoupled scalar wave equations as follows:

$$\Delta A_x + k^2 \hat{\varepsilon} A_x - \frac{\partial \log \hat{\varepsilon}}{\partial x}\frac{\partial A_x}{\partial x} = 0, \tag{9}$$

$$\Delta A_y + k^2 \hat{\varepsilon} A_y - \frac{\partial \log \hat{\varepsilon}}{\partial y}\frac{\partial A_y}{\partial y} = 0. \tag{10}$$

Two variables A_x and A_y correspond to the two polarizations.[7] The accuracy of the weakly guiding approximation is very high, the difference between the image intensities calculated by using the original 3D waveguide model and its weakly guiding approximation is <0.1%.[7]

The difference in the image intensities between the two polarizations, A_x and A_y is at most 1.6% for NA 0.33.[7] In the following discussion, we focus on the A_x polarization assuming $A_y = 0$. If high accuracy is desired, both A_x and A_y polarizations should be calculated and averaged.

The electric and magnetic fields of A_x polarization are expressed as follows:

$$E_x = ikA_x + \frac{i}{k}\frac{\partial}{\partial \mathrm{x}}\left(\frac{1}{\hat{\varepsilon}}\frac{\partial A_x}{\partial x}\right), \tag{11}$$

$$E_y = \frac{i}{k}\frac{\partial}{\partial \mathrm{y}}\left(\frac{1}{\hat{\varepsilon}}\frac{\partial A_x}{\partial x}\right), \tag{12}$$

$$H_x = 0, \tag{13}$$

$$H_y = \frac{\partial A_x}{\partial z}. \tag{14}$$

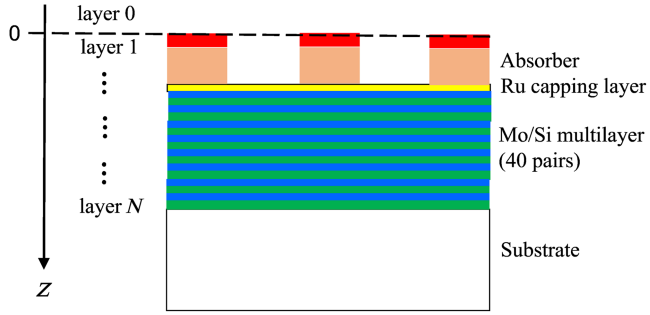

Fig. 1 Schematic view of the cross-section of an EUV mask.

We need two boundary conditions to fix the wave going forward $A_x{}^+$ and the wave going backward $A_x{}^-$. Because the electric field of A_x polarization is almost parallel to the x-axis,[7] we impose the following conditions at the boundary between the j'th and $(j+1)$th layers.

$$E_x^j(x, y, z_{j+1}) = E_x^{j+1}(x, y, z_{j+1}), \tag{15}$$

$$H_y^j(x, y, z_{j+1}) = H_y^{j+1}(x, y, z_{j+1}), \tag{16}$$

where z_{j+1} is the top of the $(j+1)$th layer. As shown in Fig. 1, we define the vacuum above the absorber as layer 0, the top absorber layer as layer 1, and the bottom of the multilayer as layer N. The z coordinate at the absorber surface is $z_1 = 0$. The boundary condition for E_y is ignored because the value is small compared with that of E_x or H_y.

2.3 Calculation of the 3D Waveguide Model in Momentum Space

2.3.1 *Eigenvalue equation*

We first apply separable approximation to the vector potential A_x to find a special solution of Eq. (9)

$$A_x(x, y, z) = F(x, y)Z(z). \tag{17}$$

Then, Eq. (9) is divided into two parts.

$$\frac{\partial^2 \mathrm{F}}{\partial x^2} + \frac{\partial^2 F}{\partial y^2} + k^2 \hat{\varepsilon} \mathrm{F} - \frac{\partial \log \hat{\varepsilon}}{\partial \mathrm{x}} \frac{\partial F}{\partial x} = \alpha^2 \mathrm{F}, \tag{18}$$

$$\frac{\mathrm{d}^2 Z}{\mathrm{d}^2 z} = -\alpha^2 Z. \tag{19}$$

In momentum space, Eq. (18) is an eigenvalue equation having an eigenvalue α. The general solution of Eq. (9) is the sum of the solutions having different eigenvalues.

We assume a periodic boundary condition having the period (d_x, d_y). Then, the momentum (k_x, k_y) has a discrete value $(2\pi l/d_x, 2\pi m/d_y)$, in which l and m are integers. In momentum space, Eq. (18) is an eigenvalue equation as follows:

$$DF = \alpha^2 F, \tag{20}$$

where D is a matrix

$$D_{lm,l'm'} = \left\{ -\left(s_x^0 + \frac{2\pi l}{d_x}\right)^2 - \left(s_y^0 + \frac{2\pi m}{d_y}\right)^2 \right\} \delta_{ll'}\delta_{mm'} + k^2 \hat{\varepsilon}_{l-l'm-m'} - \eta_{l-l'm-m'} \mathrm{i} \left(s_x^0 + \frac{2\pi l'}{d_x}\right), \tag{21}$$

where

$$\hat{\varepsilon}_{lm} = \frac{1}{d_x d_y} \int_0^{d_x} \mathrm{dx} \int_0^{d_y} \mathrm{d}y \hat{\varepsilon}(x, y) \exp\left(-i\left(\frac{2\pi l}{d_x}x + \frac{2\pi m}{d_y}y\right)\right), \tag{22}$$

$$\eta_{lm} = \frac{1}{d_x d_y}\int_0^{d_x} \mathrm{dx}\int_0^{d_y} \mathrm{dy}\frac{d\ \log\ \hat{\varepsilon}(x,y)}{dx}\ \exp\left(-i\left(\frac{2\pi l}{d_x}x+\frac{2\pi m}{d_y}y\right)\right)$$
$$= i\frac{2\pi l}{d_x}\frac{1}{d_x d_y}\int_0^{d_x} \mathrm{dx}\int_0^{d_y} \mathrm{dy}\ \log\ \hat{\varepsilon}(x,y)\exp\left(-i\left(\frac{2\pi l}{d_x}x+\frac{2\pi m}{d_y}y\right)\right). \quad (23)$$

The momentum of the chief ray (s_x^0, s_y^0) is defined by

$$s_x^0 = k\ \sin\ \theta\ \sin\ \varphi, \quad (24)$$

$$s_y^0 = k\ \sin\ \theta\ \cos\ \varphi. \quad (25)$$

The general form of the vector potential inside the jth layer A_x^j is the sum of the solutions having different eigenvalues as follows:

$$A_x^j(x,y,z) = \sum_n \left\{A_n^j\ \exp(\mathrm{i}\alpha_n^j(z-z_j)) + A_n'^j\ \exp(-i\alpha_n^j(z-z_j))\right\}$$
$$\times \sum_{lm}(F_n^j)_{lm}\exp\left(\mathrm{i}\left(s_x^0+\frac{2\pi l}{d_x}\right)x + i\left(s_y^0+\frac{2\pi m}{d_y}\right)y\right), \quad (26)$$

where α_n^j and F_n^j are the n'th eigen value and eigen vector of the matrix D^j. A_n^j and $A_n'^j$ are the amplitudes to be determined from the boundary conditions.

2.3.2 *Boundary conditions*

The boundary condition for E_x in Eq. (15) is written as follows:

$$B^j(A_n^j\gamma_n^j + A_n'^j/\gamma_n^j) = B^{j+1}(A_{n'}^{j+1} + A_{n'}'^{j+1}), \quad (27)$$

where

$$(B_n^j)_{lm} = \mathrm{i}k(F_n^j)_{lm} - \frac{i}{k}\left(s_x^0+\frac{2\pi l}{d_x}\right)\sum_{l'm'}\sigma^j_{l-l'm-m'}\left(s_x^0+\frac{2\pi l'}{d_x}\right)(F_n^j)_{l'm'}, \quad (28)$$

$$\gamma_n^j = \exp(\mathrm{i}\alpha_n^j(z_{j+1}-z_j)), \quad (29)$$

$$\sigma_{lm} = \frac{1}{d_x d_y}\int_0^{d_x}\mathrm{dx}\int_0^{d_y}\mathrm{dy}\frac{1}{\hat{\varepsilon}(x,y)}\ \exp\left(-i\left(\frac{2\pi l}{d_x}x+\frac{2\pi m}{d_y}y\right)\right). \quad (30)$$

Equation (27) can be rewritten as follows:

$$A_n^j\gamma_n^j + A_n'^j/\gamma_n^j = C^j(A_{n'}^{j+1} + A_{n'}'^{j+1}), \quad (31)$$

where

$$(C^j)_{nn'} = (B_n^j)^{-1}B_{n'}^{j+1}. \quad (32)$$

In the same way, the boundary condition for H_y in Eq. (16) is written as follows:

$$A_n^j\gamma_n^j - A_n'^j/\gamma_n^j = \frac{\alpha_{n'}^{j+1}}{\alpha_n^j}C'^j(A_{n'}^{j+1} - A_{n'}'^{j+1}), \quad (33)$$

where

$$(C'^j)_{nn'} = (F_n^j)^{-1}F_{n'}^{j+1}. \quad (34)$$

In Eqs. (31) and (33), we obtain

$$\begin{pmatrix} A_n^j \\ A_n'^j \end{pmatrix} = T^j\begin{pmatrix} A_{n'}^{j+1} \\ A_{n'}'^{j+1} \end{pmatrix}, \quad (35)$$

where T^j is a matrix which connects j'th and $(j+1)$th layers.

$$(T^j)_{nn'} = \begin{pmatrix} \frac{1}{2}\left(C^j + \frac{\alpha_{n'}^{j+1}}{\alpha_n^j} C'^j\right)/\gamma_n^j & \frac{1}{2}\left(C^j - \frac{\alpha_{n'}^{j+1}}{\alpha_n^j} C'^j\right)/\gamma_n^j \\ \frac{1}{2}\left(C^j - \frac{\alpha_{n'}^{j+1}}{\alpha_n^j} C'^j\right)\gamma_n^j & \frac{1}{2}\left(C^j + \frac{\alpha_{n'}^{j+1}}{\alpha_n^j} C'^j\right)\gamma_n^j \end{pmatrix}. \tag{36}$$

2.3.3 *Inside the multilayer and capping layer*

Inside the multilayer and capping layer, the complex dielectric constant is uniform in x-y direction.

$$\hat{\varepsilon}^j(x, y) = \hat{\varepsilon}_j. \tag{37}$$

Then, the solution of Eq. (9) is a plane wave having the momentum $k_{\mathrm{lm}}^{\mathrm{j}}$

$$k_{\mathrm{lm}}^{\mathrm{j}} = \sqrt{k^2\hat{\varepsilon}_j - \left(s_x^0 + \frac{2\pi l}{d_x}\right)^2 - \left(s_y^0 + \frac{2\pi m}{d_y}\right)^2}. \tag{38}$$

The eigenvalue α_{lm}^j and eigenvector F_{lm}^j in Eq. (20) are written as follows:

$$\alpha_{\mathrm{lm}}^j = k_{\mathrm{lm}}^{\mathrm{j}}, \tag{39}$$

$$(F_{lm}^j)_{l'm'} = \delta_{ll'}\delta_{mm'}. \tag{40}$$

The matrix T^j in Eq. (36) is

$$(T^j)_{lml'm'} = \begin{pmatrix} \frac{1}{2}\left(C^j + \frac{k_{\mathrm{lm}}^{j+1}}{k_{\mathrm{lm}}^j} C'^{\mathrm{j}}\right)/\gamma_{lm}^j & \frac{1}{2}\left(C^j - \frac{k_{\mathrm{lm}}^{\mathrm{j}+1}}{k_{\mathrm{lm}}^{\mathrm{j}}} C'^{\mathrm{j}}\right)/\gamma_{lm}^j \\ \frac{1}{2}\left(C^j - \frac{k_{\mathrm{lm}}^{j+1}}{k_{\mathrm{lm}}^{\mathrm{j}}} C'^j\right)\gamma_{lm}^j & \frac{1}{2}\left(C^j + \frac{k_{\mathrm{lm}}^{j+1}}{k_{\mathrm{lm}}^j} C'^{\mathrm{j}}\right)\gamma_{lm}^j \end{pmatrix}, \tag{41}$$

where

$$(C^{\mathrm{j}})_{lml'm'} = \frac{k - \frac{1}{k\hat{\varepsilon}_{\mathrm{j}+1}}\left(s_x^0 + \frac{2\pi l}{d_x}\right)^2}{k - \frac{1}{k\hat{\varepsilon}_j}\left(s_x^0 + \frac{2\pi l}{d_x}\right)^2}\delta_{ll'}\delta_{mm'}, \tag{42}$$

$$(\mathrm{C}'^{\mathrm{j}})_{\mathrm{lm1'm'}} = \delta_{\mathrm{ll'}}\delta_{\mathrm{mm'}}, \tag{43}$$

$$\gamma_{lm}^j = \exp(\mathrm{i}k_{\mathrm{lm}}^{\mathrm{j}}(z_{j+1} - z_j)). \tag{44}$$

2.3.4 *Boundary condition at the bottom of the multilayer*

Inside the substrate, only the forward-going wave A_x^s exists.

$$A_x^s(x, y, z) = \sum_{lm}(A_x^s)_{\mathrm{lm}} \exp(ik_{lm}^s(z - z_s)) \exp\left(\mathrm{i}\left(s_x^0 + \frac{2\pi l}{d_x}\right)x + i\left(s_y^0 + \frac{2\pi m}{d_y}\right)y\right), \tag{45}$$

where z_s is the bottom of the multilayer (top of the substrate) and k_{lm}^s is defined by

$$k_{\mathrm{lm}}^{\mathrm{s}} = \sqrt{k^2\hat{\varepsilon}_s - \left(s_x^0 + \frac{2\pi l}{d_x}\right)^2 - \left(s_y^0 + \frac{2\pi m}{d_y}\right)^2}, \tag{46}$$

where $\hat{\varepsilon}_{\mathrm{s}}$ is the complex dielectric constant of the substrate.

At the bottom of the multilayer, the boundary condition for E_x is

$$\left(\mathrm{k} - \frac{1}{k\hat{\varepsilon}_{\mathrm{N}}}\left(s_x^0 + \frac{2\pi l}{d_x}\right)^2\right)(\mathrm{A}_{\mathrm{lm}}^N\gamma_{\mathrm{lm}}^N + \mathrm{A}_{\mathrm{lm}}'^N/\gamma_{\mathrm{lm}}^N) = \left(k - \frac{1}{k\hat{\varepsilon}_{\mathrm{s}}}\left(s_x^0 + \frac{2\pi l}{d_x}\right)^2\right)(\mathrm{A}_{\mathrm{x}}^s)_{\mathrm{lm}}. \tag{47}$$

and the boundary condition for H_y is

$$k^{\mathrm{N}}_{\mathrm{lm}}(A^{N}_{lm}\gamma^{N}_{lm}-A'^{\mathrm{N}}_{\mathrm{lm}}/\gamma^{\mathrm{N}}_{\mathrm{lm}})=\mathrm{k}^{s}_{\mathrm{lm}}(\mathrm{A}^{\mathrm{s}}_{\mathrm{x}})_{\mathrm{lm}}. \tag{48}$$

In Eqs. (47) and (48), we obtain

$$\begin{pmatrix}\mathrm{A}^{\mathrm{N}}_{\mathrm{lm}}\\ \mathrm{A}'^{\mathrm{N}}_{\mathrm{lm}}\end{pmatrix}=\mathrm{T}^{\mathrm{N}}(\mathrm{A}^{\mathrm{s}}_{\mathrm{x}})_{\mathrm{lm}}, \tag{49}$$

where

$$(\mathrm{T}^{\mathrm{N}})_{lm}=\begin{pmatrix}\frac{1}{2}\left(\frac{k-\frac{1}{k\hat{\varepsilon}_{\mathrm{s}}}\left(s^{0}_{x}+\frac{2\pi l}{d_x}\right)^{2}}{k-\frac{1}{k\hat{\varepsilon}_{\mathrm{N}}}\left(s^{0}_{x}+\frac{2\pi l}{d_x}\right)^{2}}+\frac{\mathrm{k}^{s}_{\mathrm{lm}}}{\mathrm{k}^{N}_{\mathrm{lm}}}\right)/\gamma^{N}_{\mathrm{lm}}\\ \frac{1}{2}\left(\frac{\mathrm{k}-\frac{1}{k\hat{\varepsilon}_{\mathrm{s}}}\left(s^{0}_{x}+\frac{2\pi l}{d_x}\right)^{2}}{\mathrm{k}-\frac{1}{k\hat{\varepsilon}_{\mathrm{N}}}\left(s^{0}_{x}+\frac{2\pi l}{d_x}\right)^{2}}-\frac{\mathrm{k}^{s}_{\mathrm{lm}}}{\mathrm{k}^{N}_{\mathrm{lm}}}\right)\gamma^{\mathrm{N}}_{\mathrm{lm}}\end{pmatrix}. \tag{50}$$

2.3.5 *Incoming and outgoing waves in vacuum*

Assuming the periodic boundary condition, the pupil position of the outgoing wave (p_x, p_y) has a discrete value as follows:

$$(p_x, p_y)=\left(\frac{2\pi l_p}{\mathrm{d_x}}, \frac{2\pi m_p}{\mathrm{d_y}}\right), \tag{51}$$

where l_p and m_p are integers. The outgoing wave has a momentum $(s^0_x+p_x, s^0_y+p_y)$.

For convenience, we also discretize the source position as follows:

$$(s_x, s_y)=\left(\frac{2\pi l_s}{\mathrm{d_x}}, \frac{2\pi m_s}{\mathrm{d_y}}\right), \tag{52}$$

where l_s and m_s are integers. The incoming wave has a momentum $(s^0_x+s_x, s^0_y+s_y)$.

In general, the source position does not have a discrete value. The source size is $\mathrm{NA_{ill}}\times 2\pi/\lambda$, where $\mathrm{NA_{ill}}$ is the numerical aperture of the illumination optics. If the mask pitch d_x and d_y are much larger than the wavelength λ, the source positions, Eq. (52) densely cover the entire source (Fig. 2). In this case, we do not need to repeat the calculation. However, if d_x or d_y is small, the grid size becomes large, and the source positions coarsely cover the source. In this case, we need to repeat the calculation by slightly shifting the momentum of the chief ray from (s^0_x, s^0_y) to $(s^0_x+\Delta s_x, s^0_y+\Delta s_y)$, where $(\Delta s_x, \Delta s_y)$ is a fraction of one grid $(2\pi/d_x, 2\pi/d_y)$.

When the source position of the incoming wave is $(2\pi l_s/d_x, 2\pi m_s/d_y)$, the vector potential A_x at the top of the absorber surface is the sum of the incoming wave A^{+}_{x} and the outgoing wave A^{-}_{x} as follows:

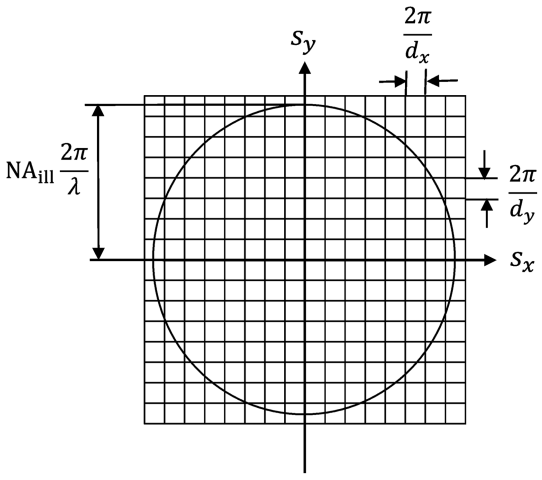

Fig. 2 Discretization of the source position.

$$A_x(x,y,z) = (\mathrm{A_x^+})_{l_s m_s} \exp\left(i\left\{\left(s_x^0 + \frac{2\pi l_s}{\mathrm{d_x}}\right)x + \left(s_y^0 + \frac{2\pi m_s}{d_y}\right)y + k_{l_s m_s} z\right\}\right) + \sum_{l_p m_p} (\mathrm{A_x^-})_{l_p m_p}^{l_s m_s} \exp\left(i\left\{\left(s_x^0 + \frac{2\pi l_p}{\mathrm{d_x}}\right)x + \left(s_y^0 + \frac{2\pi m_p}{d_y}\right)\mathrm{y} - k_{l_p m_p}\mathrm{z}\right\}\right), \quad (53)$$

where

$$k_{\mathrm{lm}} = \sqrt{\mathrm{k}^2 - \left(s_x^0 + \frac{2\pi l}{d_x}\right)^2 - \left(s_y^0 + \frac{2\pi m}{d_y}\right)^2}. \quad (54)$$

The electric field of the incoming wave is

$$(\boldsymbol{E}^+)_{l_s m_s} = \frac{i(A_\mathrm{x}^+)_{l_s m_s}}{k}\left(k^2 - \left(s_x^0 + \frac{2\pi l_s}{\mathrm{d_x}}\right)^2, -\left(s_x^0 + \frac{2\pi l_s}{\mathrm{d_x}}\right)\left(s_y^0 + \frac{2\pi m_s}{d_y}\right), -\left(s_x^0 + \frac{2\pi l_s}{d_x}\right)k_{l_s m_s}\right), \quad (55)$$

and the electric field of the outgoing wave is

$$(\boldsymbol{E}^-)_{l_p m_p}^{l_s m_s} = \frac{i(A_\mathrm{x}^-)_{l_p m_p}^{l_s m_s}}{k}\left(k^2 - \left(s_x^0 + \frac{2\pi l_p}{\mathrm{d_x}}\right)^2, -\left(s_x^0 + \frac{2\pi l_p}{\mathrm{d_x}}\right)\left(s_y^0 + \frac{2\pi m_p}{d_y}\right), \left(s_x^0 + \frac{2\pi l_p}{d_x}\right)k_{l_p m_p}\right). \quad (56)$$

In lithography simulation, we normalize the electric field of the incoming wave as

$$|(\boldsymbol{E}^+)_{l_s m_s}|^2 = 1. \quad (57)$$

So, the vector potential of the incoming wave needs to be normalized as follows:

$$(A_\mathrm{x}^+)_{l_s m_s} = \frac{1}{\sqrt{k^2 - \left(s_x^0 + \frac{2\pi l_s}{d_x}\right)^2}}. \quad (58)$$

2.3.6 *Boundary condition at the top of the absorber*

At the absorber surface where $z = z_1 = 0$, the boundary condition for E_x is

$$\left\{ik - \frac{i}{k}\left(s_x^0 + \frac{2\pi l_p}{d_x}\right)^2\right\}((\mathrm{A_x^+})_{l_s m_s}\delta_{l_p l_s}\delta_{m_p m_s} + (\mathrm{A_x^-})_{l_p m_p}^{l_s m_s}) = \sum_{\mathrm{n}} (B_\mathrm{n}^1)_{l_p m_p}(\mathrm{A_n^1} + A_\mathrm{n}'^1), \quad (59)$$

and the boundary condition for H_y is

$$k_{l_p m_p}((\mathrm{A_x^+})_{l_s m_s}\delta_{l_p l_s}\delta_{m_p m_s} - (\mathrm{A_x^-})_{l_p m_p}^{l_s m_s}) = \sum_{\mathrm{n}} \alpha_\mathrm{n}^1(A_n^1 - \mathrm{A}_n'^1)(F_n^1)_{l_p m_p}. \quad (60)$$

In Eqs. (59) and (60), we obtain

$$2\mathrm{k}_{l_p m_p}(A_\mathrm{x}^+)_{l_s m_s}\delta_{l_p l_s}\delta_{m_p m_s} = \mathrm{T}^0\begin{pmatrix} A_\mathrm{n}^1 \\ \mathrm{A}_\mathrm{n}'^1 \end{pmatrix}, \quad (61)$$

where

$$(T^0)_{l_p m_p n} = \begin{pmatrix} \frac{\mathrm{k}_{l_p m_p}}{ik - \frac{i}{k}\left(s_x^0 + \frac{2\pi l_p}{d_x}\right)^2}(\mathrm{B_n^1})_{l_p m_p} + \alpha_n^1(\mathrm{F_n^1})_{l_p m_p} & \frac{k_{l_p m_p}}{ik - \frac{i}{k}\left(s_x^0 + \frac{2\pi l_p}{d_x}\right)^2}(B_n^1)_{l_p m_p} - \alpha_\mathrm{n}^1(F_n^1)_{l_p m_p} \end{pmatrix}. \quad (62)$$

2.3.7 *Solution for the outgoing wave*

We define the matrix U^j as follows:

$$U^j = T^j T^{j+1} \cdots T^N. \tag{63}$$

Using U^j, the incoming wave A_x^+ and the wave A_x^s inside the substrate are related by

$$2\mathrm{k}_{l_p m_p}(A_{\mathrm{x}}^+)_{l_s m_s}\delta_{l_p l_s}\delta_{m_p m_s} = U^0 A_x^s. \tag{64}$$

Therefore

$$A_x^s = (\mathrm{U}^0)^{-1}(2k_{l_p m_p}(A_x^+)_{l_s m_s}\delta_{l_p l_s}\delta_{m_p m_s}). \tag{65}$$

The forward-going wave and backward-going wave at the top absorber layer are calculated by

$$\begin{pmatrix} \mathrm{A}_{\mathrm{n}}^1 \\ \mathrm{A}_{\mathrm{n}}^{\prime 1} \end{pmatrix} = \mathrm{U}^1 A_{\mathrm{x}}^{\mathrm{s}}. \tag{66}$$

Finally, the outgoing wave A_x^- is

$$(A_{\mathrm{x}}^-)_{l_p m_p}^{l_s m_s} = (A_x^+)_{l_s m_s}\delta_{l_p l_s}\delta_{m_p m_s} - \frac{1}{k_{l_p m_p}}\sum_{\mathrm{n}} \alpha_{\mathrm{n}}^1 (A_n^1 - \mathrm{A}_n^{\prime 1})(F_n^1)_{l_p m_p}. \tag{67}$$

The electric field of the outgoing wave is calculated by inserting A_x^- into Eq. (56).

2.4 Example

Figure 3 shows an example of the calculation using the 3D waveguide model. The line width is 14 nm on the wafer. The optical settings are $\lambda = 13.5$ nm, NA = 0.33, and the dipole illumination, $\sigma_{\mathrm{out}}/\sigma_{\mathrm{in}} = 0.9/0.55$ with the opening angle of 90 deg. The chief ray angle $\theta = -6$ deg and the azimuthal angle $\varphi = 0$ deg.

We assume a single absorber layer, Ta with 60-nm thickness. The Ru capping layer and Mo/Si multilayer are set according to Ref. 20.

The size of the mask area is $(d_x, d_y) = (2048\ \mathrm{nm}, 2048\ \mathrm{nm})$. The computational time to solve the 3D waveguide model is 289 s using an Intel Core i9-10920X CPU and Nvidia RTX3090 GPU. We use MAGMA library[21] to speed up the eigenvalue calculation in Eq. (20). The calculation time highly depends on the cutoff momentum. According to Ref. 13, we include the momentum (k_x, k_y), which satisfies

$$\left(\frac{|k_x|}{k_x^{\max}} + 1\right)\left(\frac{|k_y|}{k_y^{\max}} + 1\right) \le 2, \tag{68}$$

where $k_x^{\max} = k_y^{\max} = 6 \cdot NA/4 \cdot 2\pi/\lambda$. This number is 6 times larger than the size of the pupil $NA/4 \cdot 2\pi/\lambda$. When the momentum is discretized by $(2\pi/\mathrm{d}_x, 2\pi/d_y)$, there are 8705 (k_x, k_y) pairs that satisfy Eq. (68).

The region in Eq. (68) is a quasi-hyperbola that mimics the diffraction spectrum of a mask pattern consisting of vertical and horizontal lines or holes. Mask patterns are conventionally

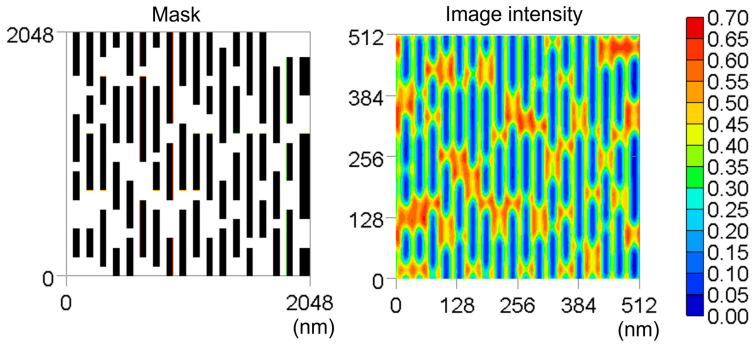

Fig. 3 Mask pattern and image intensity on a wafer.

designed using X-Y coordinates. The minimum pattern pitch in the X or Y direction is small compared with the minimum pattern pitch in the diagonal direction. Therefore, in momentum space, the diffraction amplitude in the diagonal direction decreases rapidly compared with the amplitude in the X or Y direction.

3 Linear Approximation of the Source Position Dependence of the Diffraction Amplitude

Abbe's theory, Eq. (1) can be rewritten as follows:

$$I(\boldsymbol{x}) = \iint S(\boldsymbol{s}) \left| \iint \boldsymbol{E}(\boldsymbol{k};\boldsymbol{s}) P(\boldsymbol{k}+\boldsymbol{s}) e^{i\boldsymbol{k}\cdot\boldsymbol{x}} \mathrm{d}\boldsymbol{k} \right|^2 \mathrm{d}\boldsymbol{s}, \tag{69}$$

where $\boldsymbol{k} = \boldsymbol{p} - \boldsymbol{s}$ is the scattering momentum from the incoming wave to the outgoing wave.

In optical lithography simulation, Hopkins' TCC formula[16] is often used because the computation of the TCC formula is much faster than that of Abbe's theory. In Hopkins' theory, the thin mask model is used where the diffraction amplitude is the Fourier transform (FT) of a mask pattern. The diffraction amplitude depends on the scattering momentum $\boldsymbol{k}$, but it does not depend on the source position $\boldsymbol{s}$. In this case, the TCC formula is derived by changing the order of integrations in Abbe's theory.

However, in EUV lithography simulation, the thick mask model must be used where the diffraction amplitude (electric field) $\boldsymbol{E}(\boldsymbol{k};\boldsymbol{s})$ depends on both the scattering momentum $\boldsymbol{k}$ and the source position $\boldsymbol{s}$. In this case, we cannot change the order of the integrations in Eq. (69). Therefore, the TCC formula cannot be applied to EUV lithography simulations.

To change the order of the integrations in Eq. (69), we approximate the electric field $\boldsymbol{E}(\boldsymbol{k};\boldsymbol{s})$ as a linear function of the source position $\boldsymbol{s}$ as follows:[15]

$$\boldsymbol{E}(\boldsymbol{k};\boldsymbol{s}) \cong \boldsymbol{E}(\boldsymbol{k}) + \partial_{s_x}\boldsymbol{E}(\boldsymbol{k})(s_x + k_x/2) + \partial_{s_y}\boldsymbol{E}(\boldsymbol{k})(s_y + k_y/2). \tag{70}$$

The origin of the linear expansion is $(s_x, s_y) = (-k_x/2, -k_y/2)$. The reason will be explained in Sec. 4. Inserting Eq. (70) into Eq. (69), we obtain

$$I(\boldsymbol{x}) \cong \iint S(\boldsymbol{s}) \left| \iint (\boldsymbol{E}(\boldsymbol{k}) + \partial_{s_x}\boldsymbol{E}(\boldsymbol{k})(s_x + k_x/2) + \partial_{s_y}\boldsymbol{E}(\boldsymbol{t})(s_y + k_y/2)) P(\boldsymbol{k}+\boldsymbol{s}) e^{i\boldsymbol{k}\cdot\boldsymbol{x}} \mathrm{d}\boldsymbol{k} \right|^2 \mathrm{d}\boldsymbol{s}. \tag{71}$$

Then, the order of the integrations can be changed as follows:

$$\begin{aligned} I(x) \cong & \iint TCC(\boldsymbol{k};\boldsymbol{k}')\boldsymbol{E}(\boldsymbol{k}) \cdot \boldsymbol{E}(\boldsymbol{k}')^* e^{i(\boldsymbol{k}-\boldsymbol{k}')\cdot\boldsymbol{x}} \mathrm{d}\boldsymbol{k}\, \mathrm{d}\boldsymbol{k}' \\ & + 2\,\mathrm{Re}\left\{ \iint TCC(\boldsymbol{k};\boldsymbol{k}')\boldsymbol{E}(\boldsymbol{k}) \cdot (\partial_{s_x}\boldsymbol{E}(\boldsymbol{k}')k'_x/2 + \partial_{s_y}\boldsymbol{E}(\boldsymbol{k}')k'_y/2)^* e^{i(\boldsymbol{k}-\boldsymbol{k}')\cdot\boldsymbol{x}} \mathrm{d}\boldsymbol{k}\, \mathrm{d}\boldsymbol{k}' \right\} \\ & + 2\,\mathrm{Re}\left\{ \iint TCC_x(\boldsymbol{k};\boldsymbol{k}')\boldsymbol{E}(\boldsymbol{k}) \cdot \partial_{s_x}\boldsymbol{E}(\boldsymbol{k}')^* e^{i(\boldsymbol{k}-\boldsymbol{k}')\cdot\boldsymbol{x}} \mathrm{d}\boldsymbol{k}\, \mathrm{d}\boldsymbol{k}' \right\} \\ & + 2\,\mathrm{Re}\left\{ \iint TCC_y(\boldsymbol{k};\boldsymbol{k}')\boldsymbol{E}(\boldsymbol{k}) \cdot \partial_{s_y}\boldsymbol{E}(\boldsymbol{k}')^* e^{i(\boldsymbol{k}-\boldsymbol{k}')\cdot\boldsymbol{x}} \mathrm{d}\boldsymbol{k}\, \mathrm{d}\boldsymbol{k}' \right\} \end{aligned} \tag{72}$$

where TCC, TCC_x, and TCC_y are defined by the following equations.

$$TCC(\boldsymbol{k};\boldsymbol{k}') = \iint S(\boldsymbol{s}) P(\boldsymbol{k}+\boldsymbol{s}) P^*(\boldsymbol{k}'+\boldsymbol{s}) \mathrm{d}\boldsymbol{s}, \tag{73}$$

$$TCC_x(\boldsymbol{k};\boldsymbol{k}') = \iint s_x S(\boldsymbol{s}) P(\boldsymbol{k}+\boldsymbol{s}) P^*(\boldsymbol{k}'+\boldsymbol{s}) \mathrm{d}\boldsymbol{s}, \tag{74}$$

$$TCC_y(\boldsymbol{k};\boldsymbol{k}') = \iint s_y S(\boldsymbol{s}) P(\boldsymbol{k}+\boldsymbol{s}) P^*(\boldsymbol{k}'+\boldsymbol{s}) \mathrm{d}\boldsymbol{s}. \tag{75}$$

The second-order terms in s_x and s_y are ignored in this equation. We call this formula source position-dependent TCC (STCC).[15]

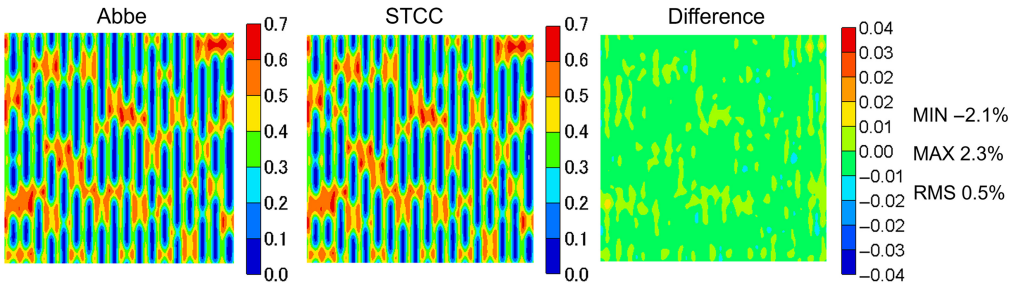

Fig. 4 Image intensities calculated using Abbe's theory and STCC formula.

The sum of coherent systems (SOCS) model[22] is conventionally used in optical lithography simulations to speed up the image intensity integration. SOCS model decomposes TCC into eigenfunctions and sums up only a small number of the eigenmodes to calculate the image intensity. SOCS model can also be applied to TCC_x and TCC_y because they are Hermitian matrices. Then, three TCCs are written as

$$\mathrm{TCC}(\boldsymbol{k};y') = \sum_n \alpha_n \varphi_n(\boldsymbol{k})\varphi_n^*(\boldsymbol{k}'), \tag{76}$$

$$\mathrm{TCC}_x(\boldsymbol{k};\boldsymbol{k}') = \sum_n \beta_n \phi_n(\boldsymbol{k})\phi_n^*(\boldsymbol{k}'), \tag{77}$$

$$\mathrm{TCC}_y(\boldsymbol{k};\boldsymbol{k}') = \sum_n \gamma_n \psi_n(\boldsymbol{k})\psi_n^*(\boldsymbol{k}'). \tag{78}$$

where α_n, β_n, and γ_n are eigenvalues and φ_n, ϕ_n, and ψ_n are eigenfunctions. These eigenvalues are real numbers.

Figure 4 compares the image intensities calculated by using Abbe's theory and the STCC formula. The optical conditions are the same as in Fig. 3. The root mean square of the image intensity difference (relative to the ML reflectivity 0.64) is very small, 0.5%. Linear approximation is a good approximation for NA 0.33 optics. Because the mask magnification is 4×, the NA on the mask side is only 0.0825. For higher NA optics, we need to confirm if this approximation is valid or not.

4 CNN for Fast EUV Lithography Simulation

4.1 M3D Parameters

The electric field of the outgoing wave $\boldsymbol{E}$ is calculated from Eq. (7) as follows:

$$\begin{aligned}\boldsymbol{E}(\boldsymbol{k};\boldsymbol{s}) &= ik\boldsymbol{A}(\boldsymbol{k};\boldsymbol{s}) - \frac{i}{k}((\boldsymbol{s}^0+\boldsymbol{p})\cdot\boldsymbol{A}(\boldsymbol{k};\boldsymbol{s}))(\boldsymbol{s}^0+\boldsymbol{p}) \\ &= ik\boldsymbol{A}(\boldsymbol{k};\boldsymbol{s}) - \frac{i}{k}((\boldsymbol{s}^0+\boldsymbol{k}+\boldsymbol{s})\cdot\boldsymbol{A}(\boldsymbol{k};\boldsymbol{s}))(\boldsymbol{s}^0+\boldsymbol{k}+\boldsymbol{s}).\end{aligned} \tag{79}$$

$\boldsymbol{E}(\boldsymbol{k})$, $\partial_{s_x}\boldsymbol{E}(\boldsymbol{k})$, and $\partial_{s_y}\boldsymbol{E}(\boldsymbol{k})$ in Eq. (70) can be calculated by expanding $\boldsymbol{A}(\boldsymbol{k};\boldsymbol{s})$ as a linear function of the source position $\boldsymbol{s}$.

Assuming the periodic boundary condition, the scattering momentum $\boldsymbol{k} = \boldsymbol{p} - \boldsymbol{s}$ has a discrete value

$$(k_x,k_y) = \left(\frac{2\pi l}{d_x},\frac{2\pi m}{\mathrm{d_y}}\right) = (p_x,p_y) - (s_x,s_y) = \left(\frac{2\pi(l_p-l_s)}{d_x},\frac{2\pi(m_p-m_s)}{d_y}\right), \tag{80}$$

where $(l,m) = (l_p - l_s, m_p - m_s)$ is the diffraction order. The vector potential $\boldsymbol{A}(\boldsymbol{k};\boldsymbol{s}) = \boldsymbol{A}(l,m;l_s,m_s)$ depends on the diffraction order (l,m) and the source position (l_s,m_s). We denote here the outgoing wave $(A_{\mathrm{x}}^-)_{l_p m_p}^{l_s m_s}$ in Sec. 2.3 as the diffraction amplitude $A_x(l,m;l_s,m_s)$. The diffraction amplitude is divided into the thin mask amplitude and the M3D amplitude as follows:

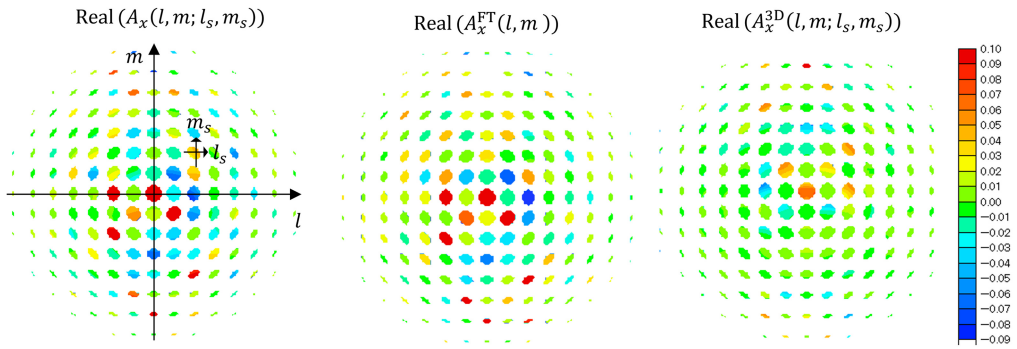

Fig. 5 Decomposition of the diffraction amplitude.

$$A_x(l,m;l_s,m_s) = A_x^{\mathrm{FT}}(l,m) + A_x^{3D}(l,m;l_s,m_s). \tag{81}$$

The thin mask amplitude $A_x^{\mathrm{FT}}(l,m)$ is calculated from the Fourier transform of the mask pattern, and it does not depend on the source position (l_s, m_s). On the other hand, the M3D amplitude $A_x^{\mathrm{3D}}(l,m;l_s,m_s)$ depends on the source position (l_s, m_s).

The contribution of the thin mask amplitude is dominant as shown in Fig. 5. The thin mask amplitude can be calculated precisely by the Fourier transformation of the mask pattern. We set the target of CNN to the residual M3D amplitude to reduce the calculation error of the total diffraction amplitude.

We assume the maximum source size $\sigma = 1$. The source area $\sigma > 1$ corresponds to the dark-field illumination, but we do not use this area in lithography. The source position and the diffraction order are restricted by the source shape and the pupil shape as follows:

$$\sqrt{l_s^2 + m_s^2} \le \frac{NA}{4}\frac{L}{\lambda}, \tag{82}$$

$$\sqrt{(l+l_s)^2 + (m+m_s)^2} \le \frac{NA}{4}\frac{L}{\lambda}. \tag{83}$$

We assume the mask size $L = d_x = d_y$. The magnification of the projection optics is 1/4.

Only the overlapping area between the pupil and the source has a possibility to contribute to the image intensity. The center of the overlapping area is $(l_s, m_s) = (-l/2, -m/2)$ as shown in Fig. 6. This is the reason why the origin of the linear expansion is $(s_x, s_y) = (-k_x/2, -k_y/2)$ in Sec. 3.

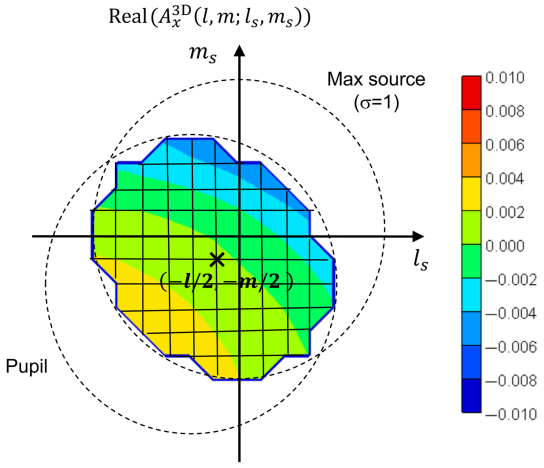

Fig. 6 Source position dependence of M3D amplitude. The diffraction order of the amplitude is (l, m). The center of the overlapping area between the source and the pupil is $(l_s, m_s) = (-l/2, -m/2)$.

The M3D amplitude $A_x^{3D}(l,m;l_s,m_s)$ smoothly depends on the source position (l_s,m_s). Although the source position dependence of the M3D amplitude is not completely linear, a linear approximation is a good approximation of the image intensity for NA 0.33 optics as discussed in Sec. 3. We approximate the M3D amplitude by a linear function of source position as follows:

$$A_x^{3D}(l,m;l_s,m_s) \cong a_0(l,m) + a_x(l,m)\,(l_s + l/2) + a_y(l,m)\,(m_s + m/2), \tag{84}$$

where $a_0(l,m)$ is the average of the amplitudes in the overlapping area and $a_x(l,m)$ and $a_y(l,m)$ are the slopes of the amplitudes in x and y directions, respectively. We call these three numbers M3D parameters.

M3D parameters are derived by least square fitting to the amplitudes at the grid points inside the overlapping area in Fig. 6. The larger (l,m), the smaller the number of the grid points inside the overlapping area. If the number of the grid points is too small the overlapping area becomes a line or just a point. In such case, we approximate the amplitude in the area using only $a_0(l,m)$ and do not use $a_x(l,m)$ and $a_y(l,m)$. Therefore, the total number of $a_0(l,m)$ is different from that of $a_x(l,m)$ or $a_y(l,m)$. When $L = 2048$ nm and NA $= 0.33$, the total number of $a_0(l,m)$ is 1901 while that of $a_x(l,m)$ or $a_y(l,m)$ is 1749.

We now go into more detail on how to calculate $A_x^{FT}(l,m)$ and $A_x(l,m;l_s,m_s)$. First, $A_x^{FT}(l,m)$ is calculated by the FT of the mask pattern using the absorber reflectance A_x^{abs} and the ML reflectance A_x^{ML}. The absorber (or ML) reflectance is calculated from $A_x(0,0;0,0)$, assuming the mask is covered (or not) by the absorber. When we insert this amplitude into Eq. (1), there is no pattern shift between the mask pattern and the image intensity at the zero-focus position. However, it is known that there is a pattern shift when EM simulations are used. This is because the effective reflection plane is inside the ML (Fig. 7).[23] Therefore, when calculating Eq. (1) with EM simulations, the pupil function P must include the defocus to compensate for this pattern shift. To be consistent with this, $A_x^{FT}(l,m)$ needs to be multiplied by a phase factor to cancel this defocusing. We assume the depth of the effective reflection plane z_{eff} to be 42 nm, which corresponds to the structure of the ML in Ref. 20.

Next, as shown in Fig. 7, the optical path length of the ray with a smaller incident angle (ray A) is shorter than the optical path length of the ray with a larger incident angle (ray B). This causes a phase difference between rays A and B, even though there is no diffraction. To exclude this effect, we multiply $A_x(l,m;l_s,m_s)$ with a phase factor $|A_x^{ML}(0,0;l_s,m_s)|/A_x^{ML}(0,0;l_s,m_s)$. This phase factor does not affect the image intensity in Eq. (1) because the total image intensity is the incoherent sum of the image intensities illuminated by different points of the effective source. This correction makes the incident angle dependence of $A_x^{3D}(l,m;l_s,m_s)$ smoother.

4.2 CNN Architecture

The input of the CNN is a mask pattern, and the outputs are M3D parameters (Fig. 8). We construct six CNNs for Real$(a_0(l,m))$, Imag$(a_0(l,m))$, Real$(a_x(l,m))$, Imag$(a_x(l,m))$, Real$(a_y(l,m))$, and Imag$(a_y(l,m))$. The total number of M3D parameters is 10,798. The larger

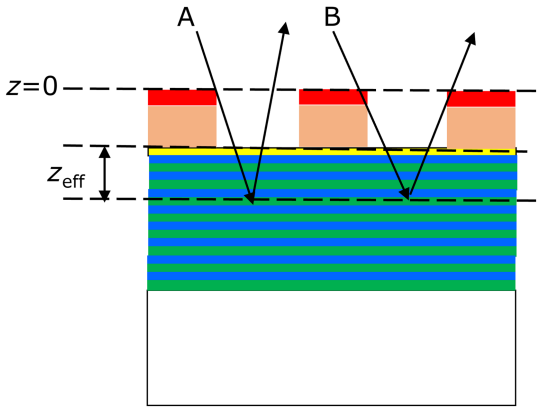

Fig. 7 Reflection of the light inside the multilayer.

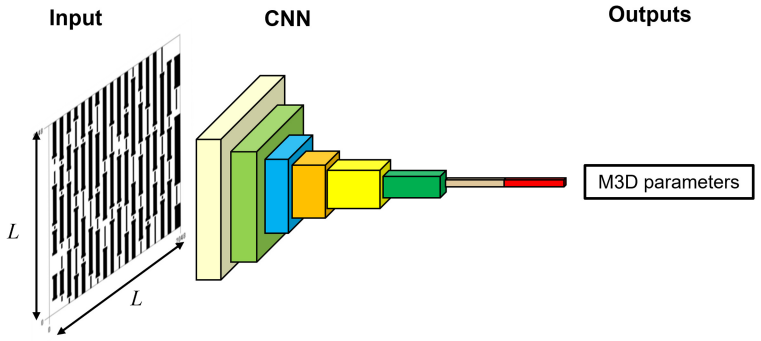

512X512
Conv2D 512X512X16
Max pooling 256X256X16
Batch normalization
Conv2D 256X256X32
Max pooling 128X128X32
Batch normalization
Conv2D 128X128X64
Max pooling 64X64X64
Batch normalization
Conv2D 64X64X128
Max pooling 32X32X128
Batch normalization
Conv2D 32X32X256
Max pooling 16X16X256
Batch normalization
Flatten 65536
Dense 4096
Dense 1901 or 1749

Fig. 8 CNN architecture.

the number of targets the harder building a CNN with high accuracy. Therefore, we split the targets into 1901 for $a_0(l,m)$ and 1749 for $a_x(l,m)$ and $a_y(l,m)$.

The input mask pattern has 2048×2048 binary data. We first convert them to 512×512 grayscale numbers by averaging the data. This is the input to CNN. Inside CNN, we repeat convolution, max pooling, and batch normalization five times. After flattening, two dense layers are added before the output.

4.3 Example

In this section, we train CNN using one million data. Figure 9 shows examples of mask patterns in the dataset. These are test patterns of metal layers. Types A, B, C, D, and E include random L/S

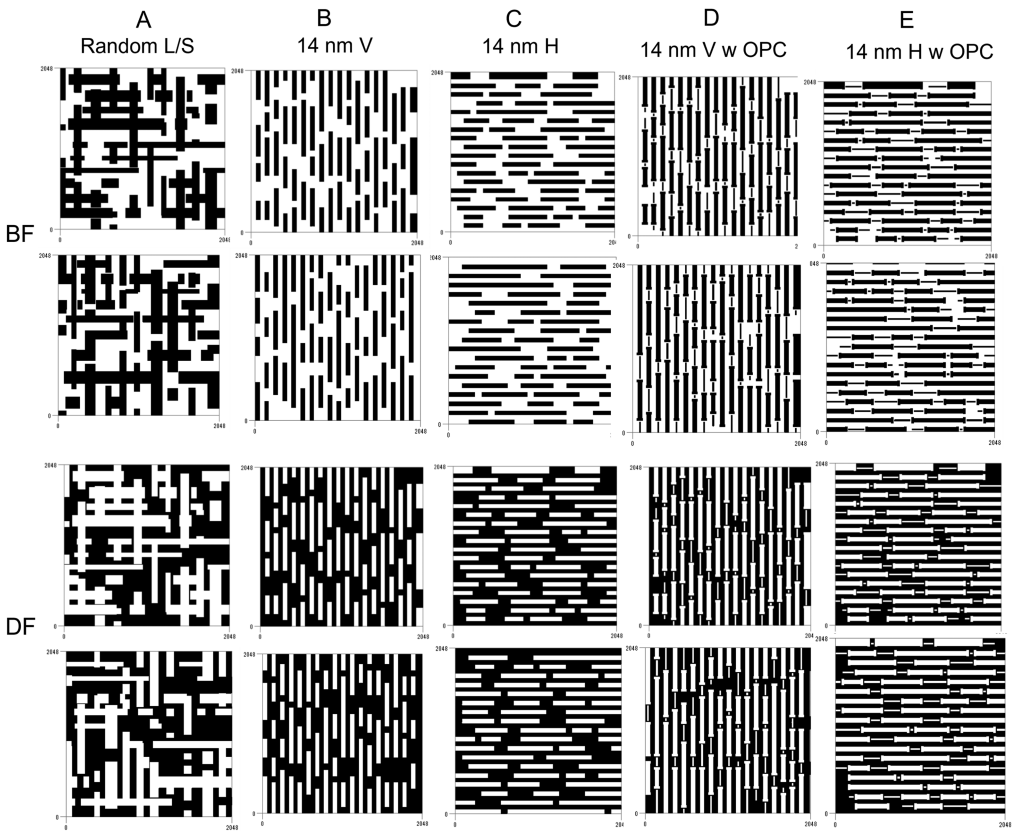

Fig. 9 Examples of mask patterns included in the dataset.

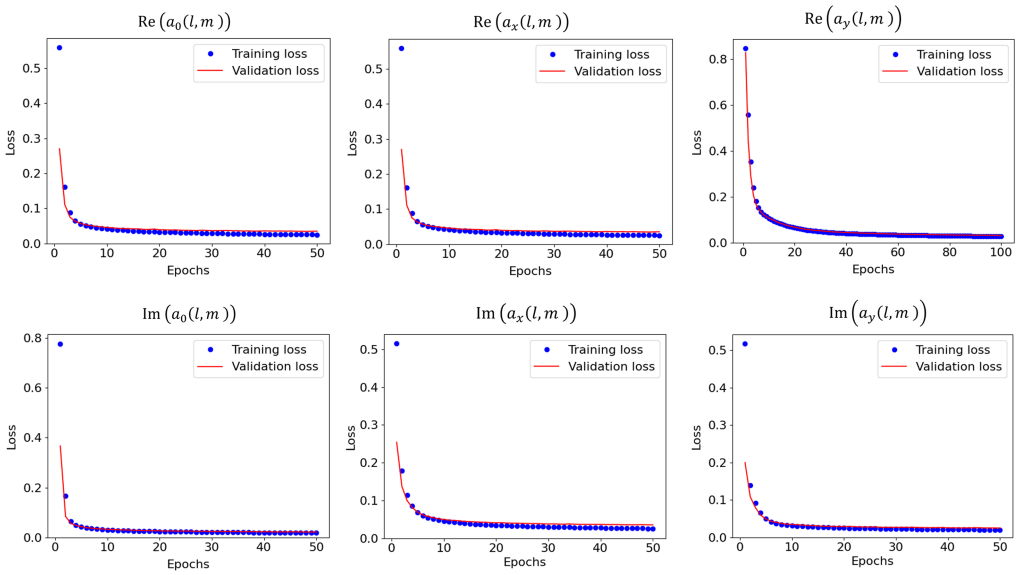

Fig. 10 Training and validation losses of CNNs for M3D parameters.

patterns, 14 nm V lines, 14 nm H lines, 14 nm V lines with OPC, and 14 nm H lines with OPC, respectively. Both the bright field (BF) patterns and the dark field (DF) patterns are included. The size of the mask pattern is 512×512 nm on the wafer. We generate 2000 original mask patterns for each mask type. Then, we use the data augmentation technique[13] to increase the amount of data by a factor of 50. In the dataset, there are 100 thousand data for each mask type and one million data in total.

Figure 10 shows the training and validation losses of six CNNs during the training. For the validation, we generate 500 mask patterns for each mask type. We do not use the data augmentation technique, and the total number of the validation data is 5000. Both the training and validation losses become small after the training. CNN successfully recognizes the characteristics of metal layers. The training time takes about 40 h using Intel Core i9-10920X CPU and Nvidia RTX3090 GPU.

After the training, we predict M3D parameters using the mask pattern in Sec. 2.4. The image intensity on a wafer is calculated by using the STCC formula in Sec. 3.

Figure 11 compares the differences in the intensities between the EM calculation and the thin mask model using FT of the mask pattern and the difference between EM and CNN prediction.

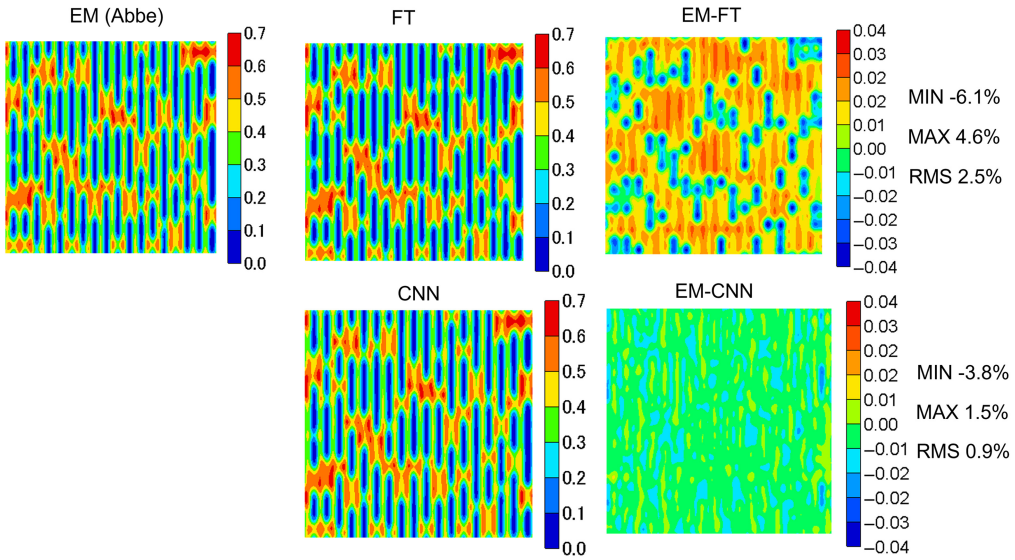

Fig. 11 Intensity difference between EM and FT, and the difference between EM and CNN.

The intensity difference between EM and CNN is much smaller than the difference between EM and FT. The root mean square of the image intensity difference between EM and FT is 2.5%, whereas the difference between EM and CNN is 0.9%.

CNN prediction time for M3D parameters is 0.05 s, and the time for image intensity integration by STCC formula is 0.07 s. The total time is 0.12 s. It is about 2400 times faster than the computation time using the 3D waveguide model with weakly guiding approximation.

The running time of CNN may not be fast enough for practical applications of OPC because it requires multiple iterations of image intensity calculations before converging. In this case, we might skip CNN calculations in the intermediate steps because the diffraction amplitude is dominated by the thin mask amplitude, which can be calculated by the Fourier transformation of the mask pattern.

5 Summary

We explain the details of our EM lithography simulator and CNN model, which reproduces the results of the EM simulations. Our EM lithography simulator uses the 3D waveguide model with weakly guiding approximation. The model solves Helmholtz-type wave equations. We extract M3D parameters representing M3D effects from the result of the EM simulation.

CNN model is constructed to predict M3D parameters from an input mask pattern. CNN prediction is much faster than EM simulation. The computation time of the EM simulation is ~5 min for 512 nm × 512 nm area on the wafer, whereas the time using CNN is ~0.1 s.

In this work, the training mask patterns for CNN were metal layers. Our final goal is to build a universal CNN for arbitrary mask patterns.

Disclosures

The authors declare there are no financial interests, commercial affiliations, or other potential conflicts of interest that have influenced the objectivity of this research or the writing of this paper.

Code and Data Availability

The codes for the simulator and CNN model are available at https://github.com/takahashi-edalab/EUVlitho.

References

1. V. Philipsen, "Mask is key to unlock full EUV potential," *Proc. SPIE* **11609**, 1160904 (2021).
2. A. Erdmann et al., "3D mask effects in high NA EUV imaging," *Proc. SPIE* **10957**, 109570Z (2019).
3. A. K. Wong and A. Neureuther, "Rigorous three-dimensional time-domain finite-difference electromagnetic simulation for photolithographic applications," *IEEE Trans. Semicond. Manuf.* **8**, 419–431 (1995).
4. M. G. Moharam and T. K. Gaylord, "Rigorous coupled-wave analysis of planar-grating diffraction," *J. Opt. Soc. Amer.* **71**, 811–818 (1981).
5. H. Tanabe, "Modeling of optical images in resists by vector potentials," *Proc. SPIE* **1674**, 637–649 (1992).
6. K. D. Lucas, H. Tanabe, and A. J. Strojwas, "Efficient and rigorous three-dimensional model for optical lithography simulation," *J. Opt. Soc. Amer. A* **13**, 2187–2199 (1996).
7. H. Tanabe, A. Jinguji, and A. Takahashi, "Weakly guiding approximation of three-dimensional waveguide model for extreme ultraviolet lithography simulation," *J. Opt. Soc. Amer. A* **41**, 1491–1499 (2024).
8. D. Gloge, "Weakly guiding fibers," *Appl. Opt.* **10**, 2252–2258 (1971).
9. S. Lan et al., "Deep learning assisted fast mask optimization," *Proc. SPIE* **10587**, 105870H (2018).
10. P. Liu, "Mask synthesis using machine learning software and hardware platforms," *Proc. SPIE* **11327**, 1132707 (2020).
11. R. Pearman et al., "Fast all-angle mask 3D ILT patterning," *Proc. SPIE* **11327**, 113270F (2020).
12. H. Tanabe, S. Sato, and A. Takahashi, "Fast EUV lithography simulation using convolutional neural network," *J. Micro/Nanopattern. Mater. Metrol.* **20**, 041202 (2021).
13. H. Tanabe and A. Takahashi, "Data augmentation in extreme ultraviolet lithography simulation using convolutional neural network," *J. Micro/Nanopattern. Mater. Metrol.* **21**, 041602 (2022).
14. H. Tanabe, A. Jinguji, and A. Takahashi, "Evaluation of convolutional neural network for fast extreme violet lithography simulation using 3 nm node mask patterns," *J. Micro/Nanopattern. Mater. Metrol.* **22**, 024201 (2023).

15. H. Tanabe, A. Jinguji, and A. Takahashi, "Accelerating extreme ultraviolet lithography simulation with weakly guiding approximation and source position dependent transmission cross coefficient formula," *J. Micro/Nanopattern. Mater. Metrol.* **23**, 014201 (2024).
16. M. Born and E. Wolf, *Principles of Optics*, 7th ed., Cambridge University Press (1999).
17. A. V. Pret et al., "Non-Gaussian CD distribution characterization for DRAM application in EUV lithography," *Proc. SPIE* **10809**, 108090A (2018).
18. D. G. Flagello, T. Milster, and A. E. Rosenbluth, "Theory of high-NA imaging in homogeneous thin films," *J. Opt. Soc. Amer. A* **13**, 53–64 (1996).
19. E. Gullikson, "CXRO X-ray database," https://henke.lbl.gov/optical_constants/.
20. N. Davydova et al., "Experimental approach to EUV imaging enhancement by mask absorber height optimization," *Proc. SPIE* **8886**, 88860A (2013).
21. S. Tomov, J. Dongarra, and M. Baboulin, "Towards dense linear algebra for hybrid GPU accelerated manycore systems," *Parallel Comput.* **36**, 232–240 (2010).
22. N. B. Cobb, "Fast optical and process proximity correction algorithms for integrated circuit manufacturing," Ph.D. dissertation, University of California, Berkeley (1998).
23. E. Setten et al., "Multilayer optimization for high-NA EUV mask3D suppression," *Proc. SPIE* **11517**, 115170Y (2020).

Hiroyoshi Tanabe is a researcher at Institute of Science Tokyo. He received his PhD degree in physics from University of Tokyo in 1986. He has more than 30 years of experience in optical and EUV lithography. He is the author of more than 30 papers. He was the program committee chair of Photomask Japan in 2003 and 2004. His current research interests include EUV masks and lithography simulation. He is a member of SPIE.

Masayuki Shimoda received the BE, ME, and DE degrees in engineering from Institute of Science Tokyo (formerly, Tokyo Institute of Technology), Tokyo, Japan, in 2018, 2020, and 2024, respectively. He is currently an assistant professor with the Department of Information and Communications Engineering of Institute of Science Tokyo. His current research interests include machine learning and VLSI physical design.

Atsushi Takahashi received his BE, ME, and DE degrees in electrical and electronic engineering from the Tokyo Institute of Technology, Tokyo, Japan, in 1989, 1991, and 1996, respectively. He is currently a professor at the Department of Information and Communications Engineering, School of Engineering, Institute of Science Tokyo. His research interests are in VLSI layout design and combinational algorithms. He is a fellow of IEICE, a senior member of IEEE and IPSJ, and a member of ACM.